Comprehensive model of the optical spectra of carbon nanotubes on a substrate by polarized microscopy

Léonard Monniello, Huy-Nam Tran, Rémy Vialla, Guillaume Prévot, Said Tahir, Thierry Michel, and Vincent Jourdain

A comprehensive model of the optical spectra of carbon nanotubes on substrate by polarized microscopy

Léonard Monniello,[1] Huy-Nam Tran,[1] Rémy Vialla,[1] Guillaume Prévot,[1] Said Tahir,[1] Thierry Michel,[1] and Vincent Jourdain[1, *]

[1]*Laboratoire Charles Coulomb (L2C), Université de Montpellier, CNRS, Montpellier, France*

Polarized optical microscopy and spectroscopy are progressively becoming key methods for the high-throughput characterization of individual carbon nanotubes (CNTs) and other one-dimensional nanostructures, on substrate and in devices. The optical response of CNTs on substrate in cross polarization experiments is usually limited by the polarization conservation of the optical elements in the experimental setup. We developed a theoretical model taking into account the depolarization by the setup and the optical response of the substrate. We show that proper modelization of the experimental data requires to take into account both non-coherent and coherent light depolarization by the optical elements. We also show how the nanotube signal can be decoupled from the complex reflection factor of the anti-reflection substrate which is commonly used to enhance the optical contrast. Finally, we describe an experimental protocol to extract the depolarization parameters and the complex nanotube susceptibility, and how it can improve the chirality assignment of individual carbon nanotubes in complex cases.

I. INTRODUCTION

One of the most fascinating aspects of single-walled carbon nanotubes (SWCNTs) is the extreme dependence of their properties on their crystalline structure and their environment. However, this remarkable feature is a two-sided coin: it opens up a wealth of new phenomena and applications[1,2] but is problematic when specific and well-controlled properties are required as for electronic applications[3]. This problem is even more acute when dealing with individual SWCNTs because measuring their structure- or environment-dependent signatures is usually long and difficult, especially when studied *in situ*[4,5] or *in operando* in devices. As a direct method of structural characterization, electron diffraction should be the method of choice for determining the structure of individual nanotubes[8] but is severely limited by the requirement of using suspended SWCNTs, and by the cost and complexity of transmission electron microscopes. In practice, Raman spectroscopy is the most popular method because it is simple to perform, is appropriate for both metallic and semiconducting SWCNTs, provides information-rich spectra and is widely available. However, a main drawback is the trial-and-error approach required to determine a laser energy in resonance with an optical transition of the studied nanotube. By measuring the optical transition energies of individual SWCNTs, resonant Rayleigh scattering represents a high-throughput method of structural identification[10] but is usually restricted to suspended nanotubes because of the intense reflection or scattering from the substrate. Recently, novel optical methods have been developed to directly measure the optical features of individual nanotubes directly on substrates.[11–13] Among them, polarized optical spectroscopy[14–16] is of particular interest since it imposes no additional constraint (*e.g.* deposited layer, liquid environment) on the sample.

The method relies on the strong polarization effect of SWCNTs along their main axis. By setting the SWCNT between two crossed polarizers, at an angle of 45° with the main axes of the polarizers, the intense substrate signal which keeps the incident polarization can be reduced by several orders of magnitude, thus making the weak nanotube signal observable (see Figure 1). The theoretical treatment is however complicated
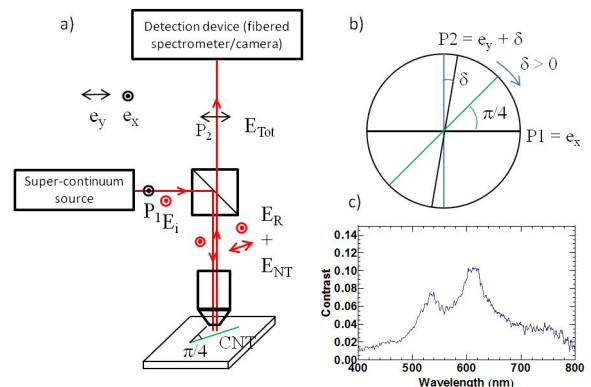

Figure 1. Polarization-based optical spectroscopy of carbon nanotubes (CNT) a) Simplified schema of the experimental setup. b) Cross polarizers configuration. Analyzer P_2 is set at an angle $\pi/2 - \delta$ with respect to the polarizer P_1 and the CNT (green line) is set at around $\pi/4$ with respect to the polarizers. c) Typical experimental spectrum of a CNT on substrate measured with $\delta = 0.02$ rad

by several factors. In their seminal article on suspended SWCNTs, Lefebvre and Finnie first took into account the interference between the nanotube signal and the transmitted light, and the imperfection of the polarization system.[14] Extending the method to SWCNTs on substrate in a reflection configuration, Liu *et al.* considered the contribution of the reflection factor of the substrate in their model with the assumption of a perfect polarization system.[15] More recently, Deng *et al.* extended the model by considering an imperfect polarization system to account for the finite contrast at small angles of crossed polarization.[16] However, even this latest model has limitations preventing it to reproduce all the experimental features and extract all the information available on the nanotube. First, it only considers non-coherent depolarization by the optical system and neglects the possibility of coherent depolarization which is needed to account for interferential features. Both types of depolarization will be described in detail in the following of the paper. Second, the complex-number nature of the reflection factor is not developed, which is especially important in the case of Si substrates with a thermal oxide

layer (SiO_2) acting as an anti-reflection coating. Such considerations are notably important because they would theoretically allow one to measure both the real and imaginary parts of the nanotube susceptibility, and not only the imaginary one as commonly done today. Very recently, F. Yao *et al* reported a method to measure the complex susceptibility on individual nanotubes using elliptical polarization[17] but this method cannot be used on the SiO_2/Si substrates which are commonly used for nanotube devices, due to the complex-number nature of the reflection coefficients. Here, we describe a model including all the above-mentioned contributions and show that it allows one to nicely reproduce the experimental spectra of SWCNTs on different substrates. We also report methods to correct the spectra from the imperfections of the optical system and to extract the real and imaginary parts of the nanotube susceptibility.

II. EXPERIMENTAL SETUP

The experimental setup is shown in figure 1a. The light source (Fianium SC-400-4, 2 ps pulses, 40 MHz) is polarized by a Glan-laser polarizer (P_1) along the axis e_x. A 80/20 beamsplitter allows illuminating the sample and collecting the signal. A microscope objective (NA 0.8, WD 1.4 mm) chosen for its polarization conservation is used to illuminate the sample. Long and aligned nanotubes (tens of microns or more) are deposited parallel to the substrate, localized by polarized optical imaging and set to be oriented at about 45° from the incident polarization whose orientation is along e_x (figure 1b). A second Glan polarizer (P_2) analyses the light from the sample which is then detected by either a camera (to image the nanotubes before acquiring their spectra) or a fibered spectrometer. P_2 is set at nearly 90° with respect to the incident polarization and the small angle of deviation is named δ. Both polarizers were chosen for their very high polarization extinction ratio (above 10^7 in optimal conditions. The scattered field from the nanotube (E_{NT}) is polarized along the nanotube axis while the field reflected by the substrate (E_r) remains polarized along the e_x direction. The diameter of the incident beam is controlled by a lens based beam reducer and an iris to improve the polarization conservation of the microscope objective by reducing the numerical aperture (NA). The typical diameter used is 2 mm for an effective NA of the incident beam of 0.4. With E_{NT}/E_R typically being in the order of 10^{-4}, nanotubes on substrate can be observed either by cutting the reflected intensity by a factor 10^8 or through interference between the reflected field and the scattered field. To detect the latter with a contrast of around 1%, one needs an extinction ratio in the order of 10^{-4} in intensity, *i.e* 10^{-2} in field. The interference signal can then be observed through a homodyne detection of the intensity on the nanotube (I) and out of the nanotube (I_0) which gives the contrast $C = (I - I_0)/I_0$. Homodyne detection is a powerful method for measuring weak optical signals: it is based on the optical interferometry between a weak optical signal and a relatively strong local-oscillator field. To account for temporal fluctuations of the laser intensity, the sample position is rapidly modulated between the two positions and the intensities are summed. This is achieved by a periodic displacement of the sample using a piezo stage (with typical displacement of 10 μm at 10 Hz), which is synchronized with the spectrum acquisition. Figure 1c shows a typical contrast spectrum of a SWNT displaying two broad features at 540 nm and 620 nm.

III. MODELISATION

We now discuss the possible models to describe the experimental spectra. First, we focus on the ideal case where the polarization of the light is conserved throughout the entire setup, as already described in reference[15]. Second, we discuss the limitations of this model and how to make it more realistic by introducing depolarization by the optical elements. Finally, we model the influence of the substrate, notably in the case of an anti-reflection layer with complex reflection and amplification factors. All angles and axes orientations used in the proposed models are defined in figure 1b.

A. Model for ideal optics.

First, let us consider the ideal case where the optical elements do not depolarize the light. The incident field $\overrightarrow{E_i}$ can be written as:

$$\overrightarrow{E_i} = |E_0|e^{ikz-i\phi}\overrightarrow{e_x} \tag{1}$$

where $|E_0|$ is the amplitude of the incident field, z is the coordinate along the axis of propagation $\overrightarrow{e_z}$, k the wave number and ϕ is the Gouy phase[18,19], the additional phase occuring in the propagation of a focused Gaussian beam. ϕ is a function of z and takes $\pi/2$ between the far field and the center of the waist, and takes another $\pi/2$ when reaching the far field. On the sample, this field is either reflected by the substrate or scattered after interacting with the CNT. As was shown for instance by Hwang *et al*[19], only the Gouy phase has influence on the resulting interference. Therefore in the following, we only consider the Gouy phase for simplicity. The reflected beam keeps the polarization of the incident beam and follows this expression:

$$\overrightarrow{E_R} = r\overrightarrow{E_i}e^{i\phi} = r|E_0|e^{i\pi}\overrightarrow{e_x} \tag{2}$$

where r is the amplitude reflection coefficient (r^2 is the reflectance). Here, the Gouy phase for the reflected beam is taken equal to π since the detection is done in the far field. The field scattered by the CNT is considered totally repolarized along the CNT axis, and writes as:

$$\overrightarrow{E_{NT}} = A\frac{(1+r)^2|E_0|e^{i\phi}}{2}(\overrightarrow{e_x} + \overrightarrow{e_y}) \tag{3}$$

where A is a complex constant which is proportional to the nanotube susceptibility χ and depends on geometrical parameters (*e.g.* the position of the CNT in the illuminated area or the collection efficiency). The $(1+r)$ factor denotes the fact

that the nanotube sees both the incident light and the reflected light. This factor is squared because this effect acts for both absorption and scattering. ϕ is the Gouy phase acquired by the field before exciting the CNT which depends on the position of the CNT within the waist: if the CNT is exactly at the beam waist, $\phi = \pi/2$. The scattered light from the CNT does not gain additional phase when going in the far field. Both fields are collected by the microscope objective and analysed through the second polarizer. The intensity I measured on the camera or the spectrometer is given by the expression:

$$I = |E_{tot}|^2 = | \left(\overrightarrow{E_R} + \overrightarrow{E_{NT}} \right) . (\sin(\delta)\overrightarrow{e_x} + \cos(\delta)\overrightarrow{e_y}) |^2 \quad (4)$$

where both fields are summed and projected on the main axis of the second polarizer which makes a small angle δ with the e_y direction (see Figure 1b). Experimentally, the angle between the main axes of the two crossed polarizers is never exactly 90°: δ defines the slight angle of deviation compared with a perfectly crossed configuration and is an important experimental parameter as shown hereafter. This intensity is compared to the reference intensity I_0 reflected by the substrate, away from the CNT:

$$I_0 = |\overrightarrow{E_R}.(\sin(\delta)\overrightarrow{e_x} + \cos(\delta)\overrightarrow{e_y})|^2 \quad (5)$$

The contrast between the two signals is given by (see SI[20] section 1A for the calculation details):

$$C = \frac{I - I_0}{I_0} \approx \frac{(1+r)^4 |A|^2}{4r^2 \delta^2} + \frac{(1+r)^2 Re(e^{i(\pi-\phi)}A^*)}{r\delta} \quad (6)$$

The first term of this equation is related to scattering and shows what would be measured in a Rayleigh scattering experiment. The second term describes the interference between the reflected field and the scattered field of the CNT. This term is called interference term in the following of this paper. If ϕ is equal to $\pi/2$, i.e the CNT is at the beam waist, then $Re(e^{i(\pi-\phi)}A^*) = Im(A)$ and we find the same expression as in reference[15]. One can see that, if the first term is negligible, the measured contrast is directly proportional to the nanotube absorption coefficient. In this case, the sign of the contrast changes with the sign of the analyzer angle (figure 2, black and red spectra). However, this is only true when δ is relatively large, which means that one needs to work at an intermediate contrast value to directly extract the absorption. At smaller angles δ it is theoretically possible to extract both $Im(A)$ and $|A|^2$, and therefore the imaginary and real parts of A, but this requires at least two measurements at different δ values.

There are however a few issues with this ideal case model when dealing with small δ angles in the range of $\pm 5.10^{-3}$ rad. First, expression (6) diverges for $\delta \rightarrow 0$ which is unphysical. Experimentally, the contrast is actually observed to decrease below a certain threshold angle value. Second, periodic oscillations experimentally appear in the contrast spectrum, which cannot be explained with this simple model. These oscillations are illustrated in figures 2a and b (blue spectra) which
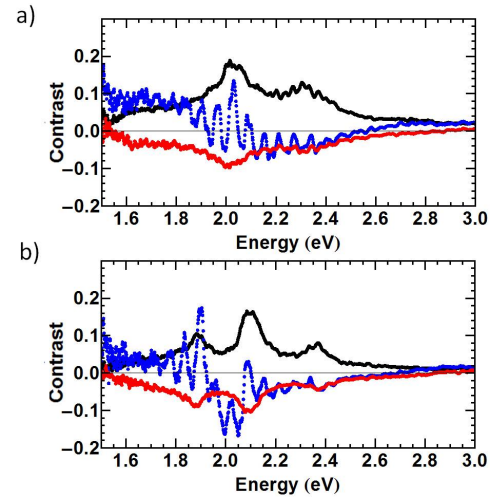

Figure 2. Experimental spectra of carbon nanotubes for three different angles δ: 10^{-2} (black), -5.10^{-3} (blue) and -5.10^{-2} (red) rad. a) Case A. b) Case B. In both cases, the substrate is 100 nm SiO$_2$/Si.

illustrate two experimental cases named cases A and B in the following.

B. Models with depolarization by the optics.

To explain these oscillations we developed a model that considers that the polarization of the incident beam on the CNT is not perfectly linear. This effect has already been partially considered in reference[16]. Here, we develop a more general model considering the two possible types of depolarization.

- Non-coherent depolarization. As in reference[16], we consider that the information contained in the polarization is lost, that is to say when part of the incident light becomes unpolarized. Because unpolarized light will not interfere with the incident or reflected fields, we call this case non-coherent depolarization. As can be found in text-books[21], unpolarized light can be modeled by two orthogonal components which are mutually incoherent. More precisely it was demonstrated that an unpolarized light electric field can be expressed in the Jones formalism as the sum of two orthogonal linearly-polarized fields with random phases[22]. Note that this is not to be confused with a truly elliptic polarization since the phase between the fields along the two axes of polarization is random. Mathematically, we used a Langevin force to model the fluctuations of the random phases so that they behave like a white noise[23], as described in detail in the SI[20] file (Annex A). The portion of the input light that is depolarized along the e_x axis (resp. the e_y axis) is called f_x (resp f_y) and is considered to be much smaller than 1. We can now write:

$$\overrightarrow{E_i} = |E_i| \left(a\overrightarrow{e_x} + f_x e^{i\psi_x(t)}\overrightarrow{e_x} + f_y e^{i\psi_y(t)}\overrightarrow{e_y} \right) \quad (7)$$

with $\psi_x(t)$ and $\psi_y(t)$ the random phases of the depolarized light. The coefficients a, f_x and f_y follow the normalization equation $|a + f_x e^{i\psi_x(t)}|^2 + |f_y e^{i\psi_y(t)}|^2 = 1$. As detailed in the SI[20], the expression of the contrast is now given by the expression:

$$C \approx \frac{(1+r)^4 |A|^2}{4r^2 \left(\delta^2 + f_y^2\right)} + \frac{\delta(1+r)^2 Re(e^{i(\pi-\phi)} A^*)}{r\left(\delta^2 + f_y^2\right)} \qquad (8)$$

One can note that by adding depolarization, expression (8) does not diverge anymore for $\delta \to 0$. In the particular case where $\phi = \pi/2$, this expression can be simplified to write:

$$C \approx \frac{(1+r)^4 |A|^2}{4r^2 \left(\delta^2 + f_y^2\right)} + \frac{\delta(1+r)^2 Im(A)}{r\left(\delta^2 + f_y^2\right)} \qquad (9)$$

This expression is similar to the one given in reference[16] and shows that non-coherent depolarization does not change the nature of the contrast. In other words, the shape of the spectra will not change. It is therefore needed to take into account another type of depolarization to account for the periodic oscillations observed at small values of δ.

- Elliptization. Here, we consider that the optical elements act as a waveplate which changes the linear polarization into an elliptic one with a fixed phase between the two orthogonal components. The portion of the input field that is depolarized is called f_{co} and is assumed to be much smaller than 1. The incident field now writes as

$$\overrightarrow{E_i} = |E_i| e^{i\phi} (\overrightarrow{e_x} + f_{co} e^{i\psi} \overrightarrow{e_y}) \qquad (10)$$

where ψ is the phase of the depolarized light. Here, contrary to the previous case, the coherently depolarized light can interfere with the input polarization when interacting with a CNT oriented at 45°. As detailed in SI[20] (part 1B), the contrast is then given by:

$$C = \frac{(1+r)^4 |A|^2}{4r^2 |\delta + f_{co} e^{i\psi}|^2} + \frac{(1+r)^2 Re\left(e^{i(\pi-\phi)} A^* (\delta + f_{co} e^{i\psi})\right)}{r|\delta + f_{co} e^{i\psi}|^2} \qquad (11)$$

By considering the particular case where $\phi = \pi/2$, one can note that A is now coupled to a complex depolarization term as can be seen in the numerator of the interference term. The complete expression can be explicited as:

$$C = \frac{(1+r)^4 |A|^2}{4r^2 |\delta + f_{co} e^{i\psi}|^2} + (1+r)^2 \frac{(\delta + f_{co} \cos\psi) Im(A) - f_{co} \sin\psi Re(A)}{r|\delta + f_{co} e^{i\psi}|^2} \qquad (12)$$

The numerator of the interference term is now composed of two contributions. The first contribution involves the nanotube absorption and is no more canceled for $\delta = 0$ but for $\delta = -f_{co} \cos\psi$ which will be named δ_0 in the following. The second contribution is related to $Re(A)$, which is itself related to $Im(A)$ through Kramers-Kronig relations[17]:

$$Re(\chi(\omega)) = \frac{2}{\pi} \int_0^\infty \frac{\omega' Im(\chi\omega'))}{\omega'^2 - \omega^2} d\omega' \qquad (13)$$

where ω is the energy. The second term in the expression of C can change drastically the shape of the contrast spectrum, providing that $\sin\psi$ is comparable to $\cos\psi$. Let us define $f = f_{co} \sin\psi$ and the expression can be written as :

$$C = \frac{(1+r)^4 |A|^2}{4r^2 |\delta - \delta_0 + if|^2} + (1+r)^2 \frac{(\delta - \delta_0) Im(A) - f Re(A)}{r|\delta - \delta_0 + if|^2} \qquad (14)$$

This expression shows that in the specific case where $f = 0$, i.e. $\psi = 0$ (or π), the contrast diverges for $\delta = \delta_0$: the two components of the polarization are in phase (or in opposition of phase) and the resulting polarization is linear. In other words, to fully model the physics behind the contrast spectrum, one must take into account both types of depolarization, coherent and non coherent, and the most general expression of the contrast is then given by :

$$C = \frac{(1+r)^4 |A|^2}{4r^2 (|\delta - \delta_0 + if|^2 + f_y^2)} + (1+r)^2 \frac{Re\left(e^{i(\pi-\phi)} A^* (\delta - \delta_0 + if)\right)}{r(|\delta - \delta_0 + if|^2 + f_y^2)} \qquad (15)$$

This expression shows the importance of knowing the type of depolarization involved in the experiment as the numerator and denominator do not have common factors. It also shows that both non-coherent and coherent depolarizations will have a coupled effect (in the denominator) and cannot be easily separated if both occur in the experiment.

C. Substrate model.

To fully model the experimental spectra, one must also take into account the effect of the substrate. In the previous part, we considered a mirror substrate with a real reflection coefficient, e.g. a silica substrate or a silicon substrate without oxide layer. In such a case, r is negative and the smaller $|r|$ is, the higher the contrast will be by both influencing the denominator term (r) and the numerator term $(1 + r)$ (see for instance
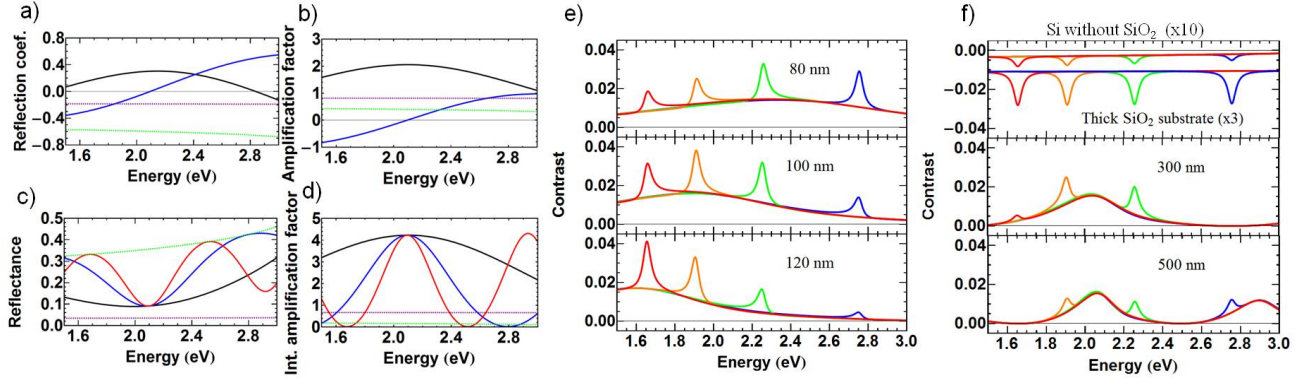
Figure 3. a) (resp. b) Evolution of the real (black line) and imaginary (blue line) part of the field reflection coefficient r_E (resp. amplification factor r_A). Green and purple dashed lines represent the coefficients of Si and SiO$_2$ substrates as references. c) (resp. d) reflectance $|r_E|^2$ (resp. amplification factor $|r_A|^2$) for three SiO$_2$ thicknesses: 100 nm (black), 300 nm (blue) and 500 nm (red). Green and purple dashed lines represent the coefficients of Si and SiO$_2$ substrates as references. e-f) Contrast obtained on different substrates considering four excitonic transitions (eq. 19).

equation (6)). In this part we will now consider the case of multilayer substrates such as SiO$_2$/Si which have been used for instance for enhancing the Raman scattering of individual nanostructures, as already reported by several groups[25–27] and can also be used in a similar way with nanotubes. This multi-layered structure leads to multiple interfering reflections which lead to two distinct coefficients. The first, r_E is the field effective reflection coefficient which is equal to r on a mirror substrate. The second, r_A, is the effective coefficient characterizing the portion of the reflected field that interacts with the CNT (i.e. $(1 + r)$ in the mirror substrate case). The latter can be seen as an amplification factor of the field interacting with the nanotube and is called "amplification factor" in the following of the paper. The interference in the oxide layer is a well known phenomenon (developed in SI[20] part 2), which causes the two reflection coefficients to become complex functions of the wavelength:

$$r_E(\lambda) = -\frac{r_{01} + r_{12}e^{2i\theta}}{1 + r_{12}r_{01}e^{2i\theta}} \qquad (16)$$

and

$$r_A(\lambda) = 1 - \frac{(1 - r_{01}^2)r_{12}e^{2i\theta}}{1 + r_{01}r_{12}e^{2i\theta}} \qquad (17)$$

where r_{01} (resp. r_{12}) is the reflection coefficient at the air/SiO$_2$ interface (resp. SiO$_2$/Si interface) and $\theta = 2n_1\pi d/\lambda$ is the dephasing due to the travel of the beam inside the oxide layer of thickness d and index n_1. The real and imaginary parts of the effective reflection coefficient are plotted as a function of the wavelength in figure 3a, for a 100 nm SiO$_2$ thickness. The reflection coefficients of silica and Si are also shown for comparison. The reflectance, $|r_E|^2$ is plotted in figure 3b for different SiO$_2$ thicknesses (100, 300 and 500 nm). The amplification factor is shown in figure 3c and the intensity amplification factor $|r_A|^2$ is shown in figure 3d. One can

observe that the behavior of the amplification factor with respect to the energy matches that of the reflection factor with opposite phase. The calculation of the contrast in the ideal case without depolarization gives a new expression (see SI[20] part 1B for details):

$$C = \frac{|A|^2|r_A|^4}{4|r_E|^2\delta^2} + \frac{Re\left(e^{i(\pi-\phi)}A^*r_A^{*2}r_E\right)}{|r_E|^2\delta} \qquad (18)$$

where one can see that the amplification factor only appears in the numerator. Its effect will add up to the one of the reflection coefficient, increasing further the contrast. Figure 3e and f illustrate the effect of the oxide thickness on the spectra. For illustration purposes, we added four CNT excitonic transitions[24,29,30] of equal strength at different energies together with a non resonant susceptibility term (i.e a complex constant A_0):

$$A(\lambda) = \frac{C_0}{(\omega_0 - \omega) - i\frac{\Gamma}{2}} + A_0 \qquad (19)$$

where ω_0 is the central frequency of a given excitonic transition, Γ its width and C_0 its amplitude. One can observe that the oxide thickness influences the profile of the background as well as the contrast of the optical transitions. The SiO$_2$ coating on Si multiplies the contrast of nanotubes by up to a factor 50 compared with silicon and by up to a factor 3 compared with fused silica (figure 4f, top). This model shows also that the thickness of the coating can be adjusted to match the energy range of the optical transitions studied (figure 4e), 80 to 100 nm giving the largest range across the visible. Figure 3f also shows that reaching higher orders of interference via a thicker oxide layer does not provides higher contrast but makes the energy range of amplification more narrow. Experimental validation of this model has been performed on 100 nm, 300 nm and 500 nm oxide thickness substrates as shown in SI[20] (part 2).

Finally, taking into account the effect of the substrate and both types of depolarization, the contrast writes as

$$C = \frac{|r_A|^4 |A|^2}{4|r_E|^2(|\delta - \delta_0 + if|^2 + f_y^2)} + \frac{Re\left(e^{i\phi} A^* r_A^{*2} r_E (\delta - \delta_0 + if)\right)}{|r_E|^2(|\delta - \delta_0 + if|^2 + f_y^2)}$$ (20)

From this expression, one can choose to use the various models previously presented. For instance, setting $f = 0$ is equivalent to have a fully non-coherent depolarization. Though this expression presents many parameters, we will see in the next part that some of them can be fixed or obtained through independent measurements. Equation (20) also highlights the importance of the Gouy phase which acts as a supplementary dephasing in the interference term. The Gouy phase is usually assumed to be equal to $\pi/2$ but note that deviations may be observed if the nanotube is not at the center of the beam waist or if the beam is not perfectly Gaussian. Importantly this final expression shows that extracting $Im(A)$ and $Re(A)$ is complexified by the coupling between A, r_E, r_A and the depolarization (δ_0 and f). This prevents a simple mathematical treatment such as dividing the contrast by the optical response of the substrate. Determining the depolarization parameters is therefore a key step to extract $Im(A)$ and $Re(A)$.

IV. FITTING, INTERPRETATION AND EXPLOITATION OF EXPERIMENTAL SPECTRA

As shown in the last two parts, the expression of the contrast is strongly modified by the depolarization by the optics and by a multi-layered substrate. To extract all possible information from the spectra, it is therefore required to know these parameters. Although the substrate is usually known well enough to be considered as a fixed parameter, it is more difficult to access the depolarization parameters. The latter ones will depend on the optical elements of the experimental setup : polarizers, beam splitter and objective. It is well known that the objective is usually the most critical optical element in a polarization microscope and the injection of the beam in the objective in terms of position, angle and width is a key aspect for polarization conservation.

From eq. (15) or (20) one can see that to extract the susceptibility of the CNT from the spectra, one first needs to determine the depolarization parameters f, f_y and δ_0. One way to access them independently from the CNT spectra is to measure the extinction ratio for each wavelength away from the nanotube (fig 4 a). To that purpose, we recorded the variation of the intensity I_0 as a function of the angle δ with the spectrometer. Assuming that $(\delta - \delta_0)$, f and f_y are all much smaller than 1, I_0 (given by the denominator of eq (20)) can be written as :

$$I_0(\omega) = |E_r(\omega)|^2 \left((\delta - \delta_0(\omega))^2 + f_y(\omega)^2 + f(\omega)^2\right)$$ (21)

where all the parameters are assumed to be dependent of the frequency ω. The intensity for each wavelength is fitted separately (fig 5 inset) to extract three parameters: $f_t^2 = f_y^2 + f^2$ from the extinction ratio (figure 4b), δ_0 from the angular deviation (figure 4c) and $|E_r|^2$ which corresponds to the spectrum with polarizers in parallel configuration. These measurements shows the excellent extinction ratio of our system in spectroscopy mode which is in the range of $0.2\text{-}0.8.10^{-4}$. One can note that both coefficients f_t^2 and δ_0 display periodic oscillations that inform about the depolarization of the light in the setup: the periodic oscillations are still observed for measurements away from the tube thus showing that the oscillations are not related to the CNT physics but to the setup characteristics, i.e depolarization features. On the one hand, the depolarization parameters f_y and f cannot be extracted independently using this characterization so that their relative influence cannot be quantitatively assessed. On the other hand, the periodic oscillations of δ_0 with the wavelength evidence coherent depolarization by the optics since δ_0 directly derives from the coherent depolarization (eq. (12) and (13)). Theoretically, such periodic oscillations of δ_0 and f with λ can be accounted for by considering that the optics act as a Michelson device with a coherent light depolarization (see SI[20] part 3).

We can now apply the proposed model to fit the experimental nanotube spectra. CNT contrast curves have been measured as a function of the angle δ following the same protocol as in the previous part. Figures 5a and b show the evolution of this contrast for the tubes in cases A and B (open circles) and for a wavelength corresponding to a maximum of the contrast (i.e an optical transition). The data are fitted using equation 20 in three cases: ideal optics ($f = \delta_0 = f_y = 0$, black line), non coherent depolarization ($f = \delta_0 = 0$, orange line), complete model with f, δ_0 and f_y different from 0. The green line displays the scattering term, extracted from the complete model which is shown to point out the domain of relevance of this term: if one works with angles below 10^{-2} rad, this term is not negligible and must be considered in the model. This threshold value for the scattering term only depends on the depolarization characteristics of the setup. If the depolarization by the setup is large, one can neglect the scattering term. One can note that having a non negligible scattering term (as in figures 5a and b) is an evidence of a good polarization conservation by the optical setup. As expected, the model with ideal optics diverges from the experimental data for small angles δ which confirms the need for a more realistic model which includes depolarization. Fitting with the non-coherent depolarization model is done by letting all parameters free except the oxide thickness which is known (in this case 100 nm). For the complete model with both types of depolarization, the large number of parameters usually precluded the convergence of the fit with all parameters free. So for illustration purposes, we assumed that the variation of the coherent depolarization parameter f, effectively a wave plate effect, was much faster than the non-coherent one f_y, which does not possess any phase component, and fixed the latter to a constant value, here 10^{-3}. This value cannot physically be fixed higher than the minimum value of f_t measured in figure 4, but can be
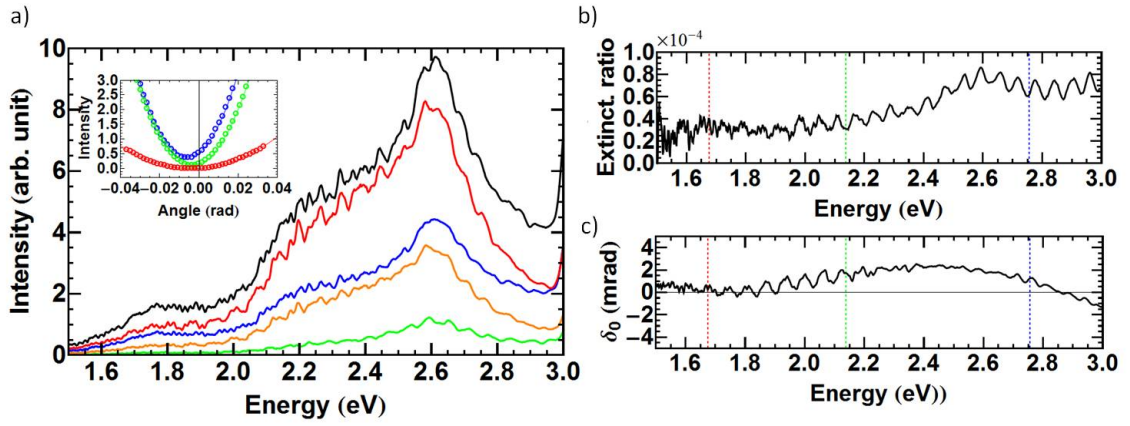
Figure 4. a) Raw spectrum on 100 nm SiO$_2$/Si substrate for different angles δ: 0.05 rad (black), 0.02 rad (blue), 0.005 rad (green), -0.02 rad (orange) -0.05 rad (red). Inset : intensity as a function of the angle for 3 wavelengths (450 nm, 580 nm and 740 nm), fitted by eq. 20 b) and c) Parameters extracted from the fitted curves: b) extinction ratio $|f_t|^2$. c) tilt angle δ_0. Vertical dotted lines show the energies used in inset.
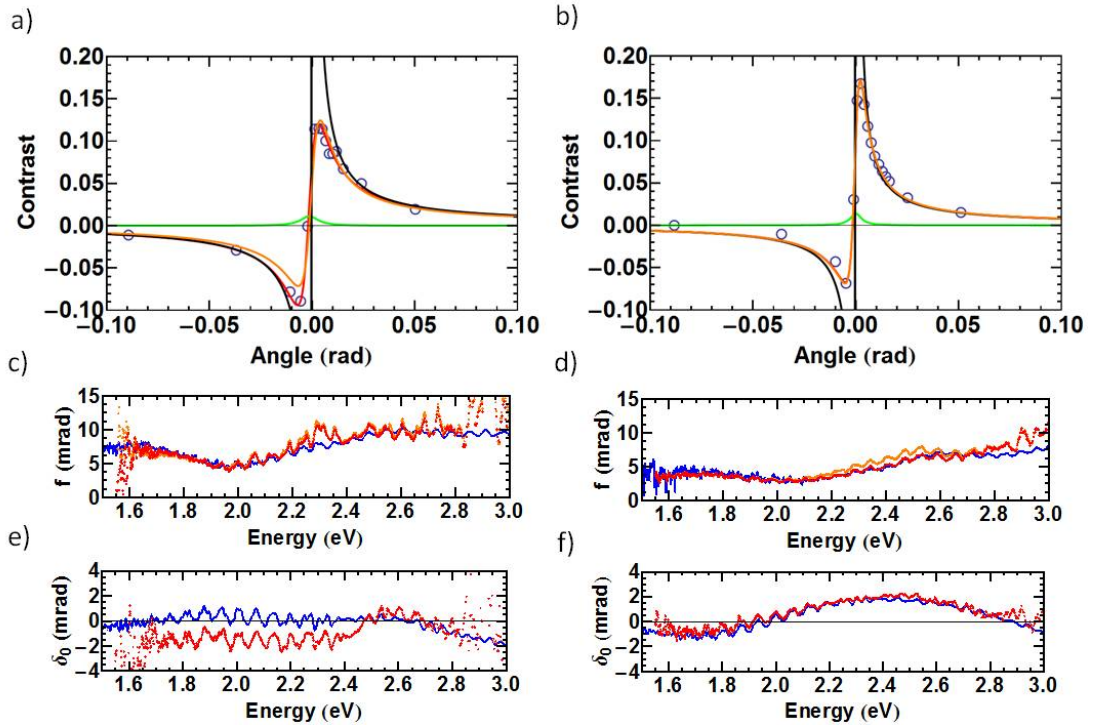

Figure 5. a) (resp. b) Contrast evolution of the tubes in case A (resp. B) for one energy corresponding to an absorption peak was selected. Black line : fit from the ideal optics model. Orange line : fit from the non-coherent depolarization model. Red line : fit from the complete model. Green line : scattering term extracted from the complete model. c-d) depolarization parameter f_t extracted from the fits (orange and red: non-coherent and complete model resp.) compared to the the data extracted beside the tube (blue). e-f) δ_0 from the complete model (red) compared to the values measured beside the tube (blue)

anywhere below it. As a matter of fact, we observed that comparable results are obtained whatever the value chosen for f_y.

As shown in figures 5a and b, the non-coherent model can satisfactorily fit the experimental data in some cases but the complete model usually provides the best fit and is required to satisfactorily fit the data in all experimental cases. Figures 5c and d (resp. e and f) display the coefficient f_t (resp. δ_0) extracted from the fit and plotted as a function of the wavelength for two experimental cases. One can observe that both models provide values of f_t reproducing very well the oscillations which were observed beside the tube (see figure 4). Therefore, this criterion alone cannot allow one to distinguish between the two models. In contrast, the complete
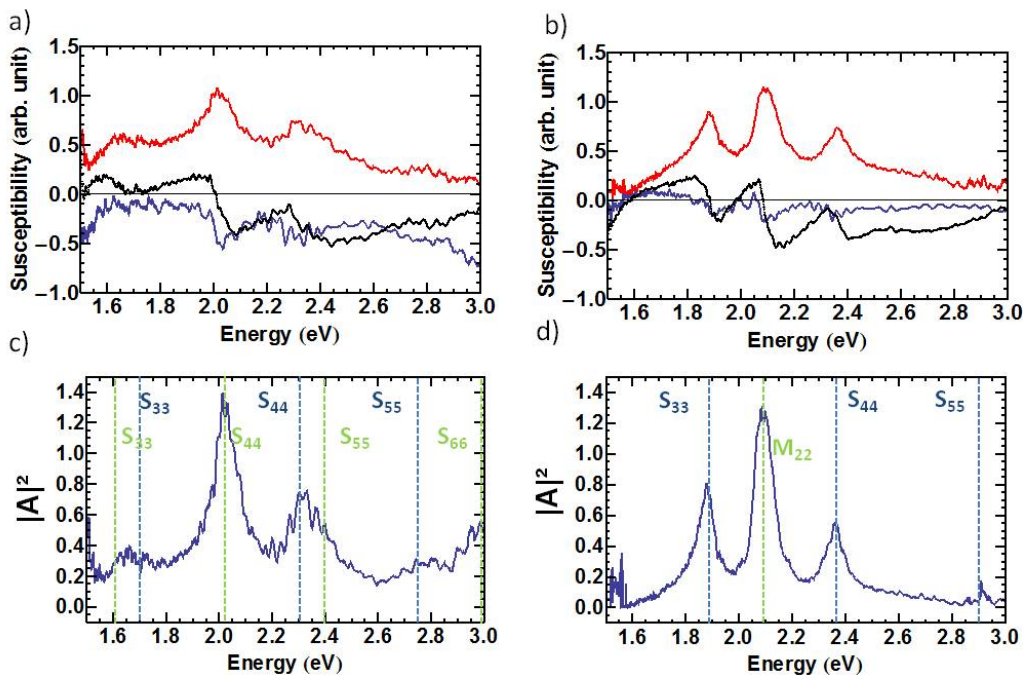
Figure 6. a) (resp.b))Susceptibility extracted for case A (resp. B) : $Re(A)$ (blue line) and $Im(A)$ (red line) extracted from the complete model. The black line represent $Re(A)$ obtained from Kramers-Kronig transformation. c) (resp.d)) $|A|^2$ extracted from the complete model for case A (resp. case B). The indexation of the resonances is described in the text.

model provides δ_0 values which accurately reproduce the variations independently measured beside the tube (see Figures 5e,f) while this parameter is intrinsically constant with the non-coherent model.

To further conclude on the relevance of both models, we plotted the two last parameters $Im(A)$ and $Re(A)$, i.e the real and imaginary parts of the susceptibility using the non coherent model and the complete model. Figures 6a and b shows the results for the complete model as it gave the best agreement. For excitonic optical transitions, it is expected that $Im(A)$ is composed of lorentzian peaks, corresponding to absorption transitions. In the common interpretation that the contrast spectrum is an absorption spectrum[15], one would expect that $Im(A)$ would look similar to the black curve on figure 2a. On that criterion, the complete model appears to be much stronger to extract $Im(A)$ than the non coherent model, which proved to be the case for every tube studied. It is also possible to compare $Re(A)$ extracted from the experimental data with the one obtained from Kramers-Kronig transformation (eq 13). One can observe a qualitative agreement of the resonances observed in both cases (see black and blue curves in Figures 6a,b), thus providing an additional support for the complete model. The remaining differences probably originate from the current limitations of the model. First, the fitting procedure could be optimized so that the f_y parameter is let free. Second, as can be seen in figures 6a and b, $Im(A)$ and $Re(A)$ still present some oscillations despite the application of the model with both depolarization types. To better address these oscillations, the model may be complexified by integrating a depolarization Michelson effect although adding more parameters may lead to convergence issues.

Extracting both $Im(A)$ and $Re(A)$ also enables one to reconstruct $|A|^2$ which is proportional to $|\chi|^2$ (Figures 6c and d), that is the Rayleigh spectrum of the nanotube. One can see that the spectrum of both figures presents the most intense peaks already visible in the raw spectra of figures 2a and have a flat background, i.e without the influence of the substrate. In particular, the substrate used (100 nm SiO_2/Si) induces a minimum of contrast at 400 nm and new features that were hidden on the spectra can now be observed. The signal-to-noise ratio is also strongly improved since the spectrum combines the data at all tilt angles. Note that it would be possible to quantitatively extract the optical susceptibility of the nanotube from the term A by experimentally measuring the beam size at each wavelength and the nanotube position in the beam as was done for instance in reference[28].

This refined optical spectrum can be used to assist and consolidate the structural assignment of carbon nanotubes by Raman spectroscopy as detailed in section 4 of the SI[20]. For instance, after treatment, the optical spectrum in case A (fig. 7c) now displays weaker resonances beside the two main resonances at around 2.0 and 2.3 eV which were already visible. Based on this information, Raman spectroscopy was directly performed at a laser energy (2.33 eV) close to the strong resonance at 2.3 eV. This yielded a semiconducting-type G-band profile and a RBM at 128 cm^{-1} corresponding to a diameter of 1.9-2.0 nm. Using a Kataura plot adapted for nan-

otubes on SiO_2 yields four possible chiralities, all being SC tubes of type 2.[31,32] Beside a S_{44} resonance at 2.3 eV, such tubes display resonances at around 1.7 eV (S_{33}) and 2.75 eV (S_{55}): resonance features are actually observed at these energies thus consolidating the interpretation. It follows that a second nanotube must be considered to account for the resonance at 2.0 eV. Raman spectroscopy was performed at a close excitation energy (1.96 eV) which yielded a semiconducting-type G-band profile with a small G- shift (about 8 cm^{-1} below G+) but no RBM: these observations agree with a type-2 SC tube with diameter of 2.2-2.3 nm (i.e. with RBM at the limit of our experimental range). Beside a S_{44} transition at 2.0 eV, such tubes have resonances at 1.6 eV (S_{33}), 2.4 eV (S_{55}) and 3 eV (S_{66}). Again, resonance features at these energies are observed after the treatment, thus confirming and consolidating the interpretation of the Raman data.

In case B, the refined optical spectrum displays three intense resonances at 1.88 eV, 2.09 eV and 2.36 eV whose profile is much more defined after treatment, together with a smaller peak at around 2.9 eV. The peaks at 1.88 eV and 2.36 eV display the asymmetric shape characteristic of Rayleigh scattering peaks, thus supporting contribution from a single resonance. The peak at 2.09 eV is more symmetric, which points toward a splitting or more than one contribution. This information was used to directly perform Raman spectroscopy at 2.33, that is close to 2.36 eV. Two low-frequency peaks at 154 cm^{-1} and 118 cm^{-1} were observed, together with a G band made of the strongly downshifted contributions of a semiconducting tube and strongly upshifted contributions of a metallic tube. All these features suggest a DWCNT made of a metallic outer tube and a semiconducting inner tube. The resonances at 1.88 eV, 2.09 eV and 2.36 eV can therefore be assigned to, respectively, the S_{33} of the inner tube, the M_{22}^-/M_{22}^+ of the outer tube, and the S_{44} of the inner tube. As detailed in SI[20], this information combined with a model of intertube coupling can be used to interpret the low-frequency modes as coupled breathing modes and refine the number of possible chiralities[33–36]: this yields different DWCNTs but all with an inner SC tube of type 2 with diameter of 1.7-1.9 nm and an outer M tube with diameter of 2.4-2.55 nm. For the outer M tube, the small splitting between M_{22}^- and M_{22}^+ (< 50 meV) points toward a near-armchair M tube (e.g. (20,17)). Such tubes are expected to display an M_{33} resonance at around 2.9 eV. For the inner SC tube, an S_{55} transition would also be expected in the range of 2.7-3 eV (depending on the energy shift induced by the intertube coupling[37] and the substrate). The weak transition 2.9 eV may therefore corresponds to these two transitions. Note that the fact that the resonance peaks are much less intense at the extremes of our energy range originates from the effect of the 100 nm SiO_2 layer which amplifies the signal in the middle of the range but reduces it at its borders.

V. CONCLUSION

We observed that the polarized optical spectra of individual carbon nanotubes are experimentally more complex than pre-viously reported. They notably display different background shapes depending on the substrate and periodic fluctuations when working at very high extinction ratio. To account for these observations, we developed a model including both coherent and non-coherent depolarization by the optics and the anti-reflection effect of the substrate. Importantly, we showed that the optical response of the substrate cannot be simply removed from the experimental spectra due to its coupling with the complex nanotube susceptibility and the coherent depolarization by the optics. We developed an experimental protocol to measure the depolarization parameters and showed that coherent depolarization is needed to correctly fit all experimental spectra: it allows to reproduce the wavelength-dependence of both the extinction ratio and the angle of maximum extinction δ_0 which would not be possible considering only non-coherent depolarization. Knowing the depolarization factors, our model allows to separate the intrinsic nanotube features from the contribution of the substrate and of the imperfect optics in the experimental mathematical spectra. Even though experimental details have to be improved, the proposed model theoretically allows to extract both the real and imaginary parts of the nanotube susceptibility even on substrates with an antireflection layer such as standard SiO_2/Si. The method may notably be improved by reducing the coherent depolarization by the optics, improving the fitting algorithm and/or explicitly considering a depolarizing Michelson effect in the model.

VII. SUPPORTING INFORMATION

Details on the mathematical development of the models and on the Raman measurements.

* vincent.jourdain@umontpellier.fr

[1] R. Zhang, Y. Zhang and F. Wei, Horizontally Aligned Carbon Nanotube Arrays: Growth Mechanism, Controlled Synthesis, Characterization, Properties and Applications. Chem. Soc. Rev. 46, 3661–3715 (2017)

[2] M. F. L. De Volder, S. H. Tawfick, R. H. Baughman and A. J. Hart, Carbon Nanotubes: Present and Future Commercial Applications. Science 339, 535 (2013)

[3] D. Jariwala, V. K. Sangwan, L. J. Lauhon, T. J. Marks and M. C. Hersam, Carbon Nanomaterials for Electronics, Optoelectronics, Photovoltaics, and Sensing. Chem. Soc. Rev. 42, 2824–2860 (2013)

[4] R. Rao, D. Liptak, T. Cherukuri, B. I. Yakobson and B. Maruyama, In situ evidence for chirality-dependent growth rates of individual carbon nanotubes, Nature Materials, vol. 11, pages 213-216 (2012)

[5] M. Picher, E. Anglaret, R. Arenal and V. Jourdain, Self-deactivation of single-walled carbon nanotube growth studied by in situ Raman measurements, Nano Lett., 9(2), pp 542-547 (2009)

[6] H. Mehedy, J. Ravaux, S. Tahir, R. Podor and V. Jourdain, In situ study of single-walled carbon nanotube growth in an environmental scanning electron microscope, Nanotechnology 27(50), 505701 (2016)

[7] H. Mehedy, J. Ravaux, K. Yazda, S. Tahir, M. Odorico, R. Podor and V. Jourdain, Increased chemical reactivity of single-walled carbon nanotubes on oxide substrate: in situ imaging and effect of electron and laser irradiations, Nano Research, 9(2), 517-529 (2016)

[8] A. Ghedjatti, Y. Magnin, F. Fossard, G. Wang, H. Amara, E. Flahaut, J.-S. Lauret and A. Loiseau, Structural Properties of Double-Walled Carbon Nanotubes Driven by Mechanical Interlayer Coupling, ACS Nano, 11, 4840–4847 (2017)

[9] R. Saito, M. Hofmann, G. Dresselhaus, A. Jorio and M. S. Dresselhaus, Raman spectroscopy of graphene and carbon nanotubes, Advances in Physics, 60:3, 413-550 (2011)

[10] M. Y. Sfeir, F. Wang, L. Huang, C.-C. Huang, J. Hone, S. O'Brien, T. F. Heinz and L. E. Brus, Probing Electronic Transitions in Individual Carbon Nanotubes by Rayleigh Scattering. Science, 306, 1540 (2004)

[11] D. Y. Joh, L. H. Herman, S.-Y. Ju, J. Kinder, M. A. Segal, J. N. Johnson, G. K. L. Chan and J. Park, On-Chip Rayleigh Imaging and Spectroscopy of Carbon Nanotubes, Nano Lett., 11, 1–7 (2010)

[12] W. Wu, J. Yue, X. Lin, D. Li, F. Zhu, X. Yin, J. Zhu, J. Wang, J. Zhang, Y. Chen, X. Wang, T. Li, Y. He and X. Dai, True-Color Real-Time Imaging and Spectroscopy of Carbon Nanotubes on Substrates Using Enhanced Rayleigh Scattering, Nano Res., 8, 2721–2732 (2015)

[13] R. W. Havener, A. W. Tsen, H. Cheul Choi and J. Park, Laser-based imaging of individual carbon nanostructures, Npg Asia Materials, vol 3., 91-99 (2011)

[14] J. Lefebvre and P. Finnie, Polarized Light Microscopy and Spectroscopy of Individual Single-Walled Carbon Nanotubes, Nano Res., 4, 788 (2011)

[15] K. Liu, X. Hong, Q. Zhou, C. Jin, J. Li, W. Zhou, J. Liu, E. Wang, A. Zettl and F. Wang, High-Throughput Optical Imaging and Spectroscopy of Individual Carbon Nanotubes in Devices, Nat Nano, 8, 917–922 (2013)

[16] S. Deng, J. Tang, L. Kang, Y. Hu, F. Yao, Q. Zhao, S. Zhang, K. Liu, and J. Zhang, High-Throughput Determination of Statistical Structure Information for Horizontal Carbon Nanotube Arrays by Optical Imaging, Adv. Mater., 28, 2018–2023 (2016)

[17] F. Yao, C. Liu, C. Chen, S. Zhang, Q. Zhao, F. Xiao, M. Wu, J. Li, P. Gao, J. Zhao, X. Bai, S. Maruyama, D. Yu, E. Wang, Z. Sun, J. Zhang, F. Wang, and K. Liu, Measurement of complex optical susceptibility for individual carbon nanotubes by elliptically polarized light excitation, Nature Comm 9:3387 (2018)

[18] L. G. Gouy, "Sur une propriete nouvelle des ondes lumineuses", C. R. Acad. Sci. Paris 110, 1251 (1890)

[19] J. Hwang and W. E. Moerner, Interferometry of a single nanoparticle using the Gouy phase of a focused laser beam. Optics Comm, 280, 487-491 (2007)

[20] See Supplemental Material at [URL] for details on the mathematical development of the models and on the Raman measurements

[21] M. Born and E. Wolf, *Interference and diffraction with partially coherent light*. In *Principles of Optics: Electromagnetic Theory of Propagation, Interference and Diffraction of Light (pp. 554-632)* (1999)

[22] W. Jizhong, *A matrix method for describing unpolarized light and its applications. Acta Mechanica Sinica, 2(4), 362-372* (1986)

[23] J. Bylander, I. Robert-Philip and I. Abram, Interference and correlation of two independent photons, Eur. Phys. J. D **22**, 295-301 (2003)

[24] S. Berciaud, C. Voisin, H. Yan, B. Chandra, R. Caldwell, Y. Shan, L. E. Brus, J. Hone and T. F. Heinz, Excitons and high-order optical transitions in individual carbon nanotubes: A Rayleigh scattering spectroscopy study, Phys Rev. B 81, 041414(R) (2010)

[25] Y. Y. Wang, Z. H. Ni, Z. X. Shen, Interference enhancement of Raman signal of graphene, Appl. Phys. Lett., 92, 043121 (2008)

[26] D. Yoon, H. Moon, Y.-W. Son, J. S. Choi, B. H. Park, Y. H. Cha, Y. D. Kim, H. Cheong, Interference effect on Raman spectrum of graphene on SiO_2/Si. Phys. Rev. B 80, 125422 (2009)

[27] H. Zhang, Y. Wan, Y. Ma, W. Wang, Y. Wang and L. Dai, Interference effect on optical signals of monolayer MoS2, Appl. Phys. Lett., 107, 101904 (2015)

[28] K. Liu, X. Hong, S. Choi, C. Jin, R. B. Capaz, J. Kim, W. Wang, X. Bai, S. G. Louie, E. Wang, F. Wang, Systematic determination of absolute absorption cross-section of individual carbon nanotubes, PNAS May 27, 111 (21), 7564-7569 (2014)

[29] R. W. Boyd, *Nonlinear Optics*, Elsevier Science, 2008

[30] H. N. Tran, J.-C. Blancon, J.-R. Huntzinger, V. N. Popov, A. A. Zahab, A. Ayari, A. San-Miguel, F. Vallée, N. Del Fatti, J.-L. Sauvajol a,d M. Paillet, Excitonic optical transitions characterized by Raman excitation profiles in single-walled carbon nanotubes, Phys Rev B 94, 075430 (2016)

[31] D. Zhang, J. Yang, F. Yang, R. Li, M. Li, D. Ji and Y. Li, (n,m) Assignments and quantification for single-walled carbon nanotubes on SiO2/Si substrates by resonant Raman spectroscopy, Nanoscale, 28;7(24):10719-27 (2015)

[32] P. Petit, D. Salem, M. He, M. Paillet, R. Parret, J.-L. Sauvajol and A. Zahab, Study of the Thermal Stability of Supported Catalytic Nanoparticles for the Growth of Single-Walled Carbon Nanotubes with Narrow Diameter Distribution by Chemical Vapor Deposition of Methane, J. Phys. Chem. C, 116 (45), pp 24123–24129 (2012)

[33] V. N. Popov, Curvature effects on the structural, electronic and optical properties of isolated single-walled carbon nanotubes within a symmetry-adapted non-orthogonal tight-binding model, New J. Phys., **6** 17 (2004)

[34] V. N. Popov ad L. Henrard, Comparative study of the optical properties of single-walled carbon nanotubes within orthogonal and nonorthogonal tight-binding models, Physical Review B, 70(11): p. 115407. (2004)

[35] H. N. Tran, D. I. Levshov, V. C. Nguyen, M. Paillet, R. Arenal, X. T. Than, A. A. Zahab, Y. I. Yuzyuk, N. M. Phan and J.-L. Sauvajol, Intrinsic phonon properties of double-walled carbon nanotubes, Adv. Nat. Sci.: Nanosci. Nanotechnol. 8 (2017) 015018.

[36] D. I. Levshov, T. Tanh, R. Arenal, V. Popov, R. Parret, M. Paillet, V. Jourdain, A. Zahab, T. Michel, Y. T. Yuzyuk and J.-L. Sauvajol, Experimental evidence of a mechanical coupling between layers in an individual double-walled carbon nanotube Nano Lett., 11 (11), 4800-4804 (2011)

[37] K. Liu, C. Jin, X. Hong, J. Kim, A. Zettl, E. Wang and F. Wang, Van der Waals-coupled electronic states in incommensurate double-walled carbon nanotubes, Nature Physics volume 10, pages 737–742 (2014)